






# Thermal equation of state of rhodium to 191 GPa and 2700 K using double-sided flash laser heating in a diamond anvil cell

J. D. McHardy <sup>\*</sup>, C. V. Storm , M. J. Duff, C. M. Lonsdale , G. A. Woolman , and M. I. McMahon   
 SUPA, School of Physics and Astronomy, and Centre for Science at Extreme Conditions, The University of Edinburgh,  
 Peter Guthrie Tait Road, Edinburgh EH9 3FD, United Kingdom

N. Giordano 

Deutsches Elektronen-Synchrotron DESY, Notkestr. 85, 22607 Hamburg, Germany

S. G. MacLeod 

AWE, Aldermaston, Reading, RG7 4PR, United Kingdom and SUPA, School of Physics and Astronomy, and Centre for Science at Extreme Conditions, The University of Edinburgh, Peter Guthrie Tait Road, Edinburgh EH9 3FD, United Kingdom



(Received 30 October 2023; revised 15 February 2024; accepted 23 February 2024; published 21 March 2024)

The phase behavior of rhodium (Rh) metal has been studied to 191 GPa and 2700 K using a combination of room-temperature isothermal compression and double-sided flash laser heating experiments. The isothermal compression data have been fitted with a second-order adapted polynomial of order  $L$  equation of state (EoS) with best-fitting parameters of  $V_0 = 13.764(2) \text{ \AA}^3/\text{atom}$ ,  $K_0 = 258(3) \text{ GPa}$ , and  $K' = 5.36(9)$ . Two-dimensional maps of the uniaxial stress component  $t$  are presented for Rh at different pressures showing the spatial distribution of the local stress state of a relatively high-yield strength material encased in a Bi pressure medium. In addition, a simple, thermal pressure equation-of-state model, based on a single Einstein temperature, has been fitted to the high-pressure-temperature data up to 2700 K at 148 GPa and ambient-pressure thermal expansion data up to 1982 K. Also determined are the best-fitting parameters to reproduce the thermal EoS within the DIOPTAS two-dimensional integration software. The optimized DIOPTAS parameters are  $V_0 = 13.764 \text{ \AA}^3/\text{atom}$ ,  $K_0 = 260.54 \text{ GPa}$ ,  $K' = 5.114$ ,  $\alpha_T = 2.99 \times 10^{-5} \text{ K}^{-1}$ ,  $\partial\alpha_T/\partial T = 1.27 \times 10^{-9} \text{ K}^{-2}$ ,  $\partial K_0/\partial T = -6.43 \times 10^{-5} \text{ GPa/K}$ , and  $\partial K'/\partial T = -9.3 \times 10^{-10} \text{ K}^{-1}$ .

DOI: [10.1103/PhysRevB.109.094113](https://doi.org/10.1103/PhysRevB.109.094113)

## I. INTRODUCTION

Rhodium (Rh) is one of six transition metals [along with ruthenium (Ru), palladium (Pd), osmium (Os), iridium (Ir), and platinum (Pt)] that form the platinum group of elements. Together with silver (Ag) and gold (Au), these elements constitute the noble metals of the periodic table as they are generally resistant to corrosion and oxidation even at elevated temperatures. As such, and despite its scarcity, Rh finds wide-ranging applications in industry, for example, as a strengthening component in alloys, in high-temperature thermocouples [1], in catalytic reduction processes [2], or even as a nanoparticle electrocatalyst component for green energy hydrogen production [3].

Despite its numerous industrial applications, relatively few experimental studies extending into the high-pressure-temperature (high- $P$ - $T$ ) regime have been performed on pure

Rh. Single-shock experiments along the principal Hugoniot have accessed states up to  $\sim 200 \text{ GPa}$  [4] while three diamond anvil cell (DAC) studies have compressed Rh to  $\sim 64 \text{ GPa}$  [5],  $\sim 83 \text{ GPa}$  [6], and  $\sim 60 \text{ GPa}$  [7] at room temperature all using a Ne pressure medium. Theoretical work suggests Rh exhibits a simple phase diagram, maintaining its face-centered-cubic (fcc) structure from ambient conditions up to pressures as high as at least  $500 \text{ GPa}$  [8] or even  $10 \text{ TPa}$  [9].

Rh's simple behavior, and its inertness at high- $T$ , make it an ideal candidate as an x-ray coupler in new experiments being developed at next-generation, hard x-ray, free electron laser (XFEL) sources [10]. In these experiments, controlled heating of low- $Z$  samples (e.g.,  $\text{H}_2\text{O}$  or  $\text{N}_2$ ) can be achieved through energy transfer from a surrounding higher- $Z$  coupler, which is itself heated by a train of XFEL x-ray pulses. The uniformity of the x-ray heating within the coupler, and therefore the low- $Z$  sample, depends on the careful selection of the coupler's x-ray absorption length, heat capacity, and heat conduction properties. For example, high- $Z$  couplers (e.g., Au) develop very large temperature gradients as a result of their short x-ray attenuation lengths, which produce nonuniform heating of the low- $Z$  sample. In contrast, a mid- $Z$  coupler like Rh achieves a more uniform temperature gradient, resulting in more homogeneous heating of the sample. In addition, Rh's thermal conductivity allows sufficient heat flow into the low- $Z$

\*J.D.McHardy@ed.ac.uk

sample while not being so high that the heat is preferentially dissipated within the coupler itself; its high melting temperature (2242 K at ambient pressure, increasing to  $> 6900$  K at 150 GPa [9]) enables extreme  $P$ - $T$  states to be reached in the coupler without reaching melt; Rh's low thermal expansion limits the thermal pressure buildup within the DAC under high- $T$  conditions, thereby minimizing the pressure waves that are generated through rapid x-ray energy deposition [11].

Despite being an almost ideal coupler material, little is known about the behavior of Rh at extended  $P$ - $T$  conditions, an accurate thermal equation of state (EoS) is required if it is to be used more widely. Here we present the results of DAC experiments in which Rh was isothermally compressed to 191 GPa in a Bi pressure-transmitting medium (PTM) at 298 K and high-pressure laser heating experiments to 148 GPa and 2700 K in an MgO PTM. The data are used to refine a thermal equation-of-state model describing the pressure-volume-temperature ( $P$ - $V$ - $T$ ) behavior of the metal up to these extreme conditions. This will enable Rh to be used as a calibration standard in DAC experiments as well as a coupler in low- $Z$  heating experiments at XFELs.

## II. EXPERIMENTAL DETAILS

### A. 298-K isothermal compression

#### 1. Sample preparation

For the room-temperature compression data, two Boehler-Almax plate DACs [12], fitted with tungsten (W) gaskets and either flat 300- $\mu\text{m}$  culets (cell RT1) or 300- $\mu\text{m}$  culets beveled down to 100  $\mu\text{m}$  (RT2), were prepared. The sample loaded was high-purity Rh powder ( $> 99.95\%$ ) from Sigma-Aldrich, and the PTM and internal pressure standard [13] was Bi powder ( $> 99.999\%$ ) from Alfa Aesar. The initial gasket holes, with diameters of 100 and 37  $\mu\text{m}$  for RT1 and RT2, respectively, and thicknesses of 30 and 10  $\mu\text{m}$ , were filled with Bi powder which was then gently compacted. A second sample chamber, of a smaller diameter (35 and 13  $\mu\text{m}$  for RT1 and RT2, respectively), was then drilled partway through the Bi, thereby creating a well into which a small granule of Rh powder was placed [Fig. 1(a)]. The Rh was then covered with additional Bi such that it was entirely encased within the PTM. The initial thicknesses of the Bi PTM layers above and below the Rh sample were approximately 10 and 3  $\mu\text{m}$  for RT1 and RT2, respectively.

#### 2. XRD data collection

The ambient temperature compression data were collected on beamline ID27 of the European Synchrotron Radiation Facility (ESRF-EBS) in Grenoble, France. Two-dimensional (2D) XRD images were collected on an EIGER2 X CdTe 9M detector using an x-ray wavelength of 0.3742  $\text{\AA}$  and a beam size (FWHM) of  $1.7 \times 1.7 \mu\text{m}^2$  [14]. The detector had a pixel size of  $75 \times 75 \mu\text{m}^2$  and was located  $\sim 212$  mm from the sample. The precise sample-detector distance and tilt orientations were determined using a  $\text{CeO}_2$  standard and refinement within the detector calibration suite in DIOPTAS [15]. Data were collected at pressure intervals ranging between 2–10 GPa and following each pressure increase, the system was allowed to equilibrate for a minimum of 5 min prior to data collection.

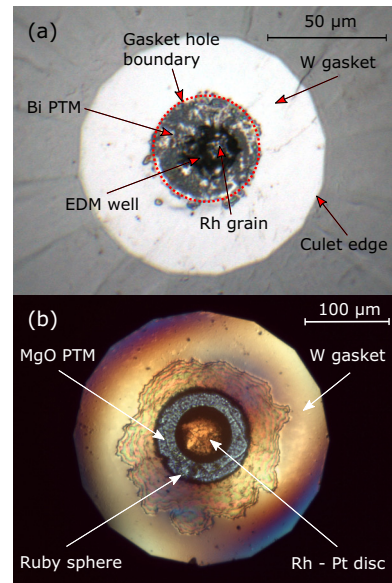


FIG. 1. Micrographs of the sample chambers in DACs RT1 and LH1. (a) Shows the loading of the Rh inside the “well” fabricated through electrical discharge machining (EDM) in the Bi PTM in RT1 before a top layer of Bi was added and the cell closed. (b) Shows DAC LH1 prior to laser heating containing a Rh disk, coated on each side with 1  $\mu\text{m}$  of Pt, encased in a MgO PTM. A ruby sphere was added beside the disk as an additional pressure marker. Some extrusion of the MgO PTM out of the sample chamber before being trapped between the W gasket and the diamond culet is evident.

At each pressure step, a grid scan of data points was collected over the sample such that the local pressure environment could be closely monitored. Typically, these scans comprised a grid of  $7 \times 7$  points spaced by 1.67  $\mu\text{m}$  which covered the Rh sample area. Wider grids of  $21 \times 21$  points across the full anvil culet were also performed at  $\sim 50$  GPa intervals. Two examples of the high-quality raw 2D x-ray diffraction (XRD) patterns collected are illustrated in Figs. 2(a) and 2(b) where the corresponding one-dimensional (1D) integrated patterns [Figs. 2(c) and 2(d)] show between 15 and 11 resolvable peaks for Bi and Rh, respectively, at low pressure, and 12 and 10 peaks at the highest pressures studied. The contrasting compressibilities of Bi and Rh resulted in some peak overlap in the integrated patterns over the pressure range studied but due to the Bi (bcc) and Rh (fcc) having different structures, this was kept to a minimum.

### B. High-temperature, double-sided laser heating

#### 1. Sample preparation

The laser heating experiment also used two Boehler-Almax plate DACs equipped with W gaskets and either 300- $\mu\text{m}$  diameter culet diamonds (LH1) or 300- $\mu\text{m}$  culets beveled to 100- $\mu\text{m}$  diameter (LH2). Both DACs were loaded with high-purity ( $> 99.9\%$ ), 6.4(2)- $\mu\text{m}$ -thick Rh foil obtained from Goodfellow. Before loading, vapor deposition was used to coat both sides of the Rh foil with 0.9(1)  $\mu\text{m}$  of Pt. The Pt coatings were applied in two  $\sim 0.45$ - $\mu\text{m}$  layers, and the foil was rotated 90° between layers in order to avoid tension buildup on the surface. These Pt layers served as the

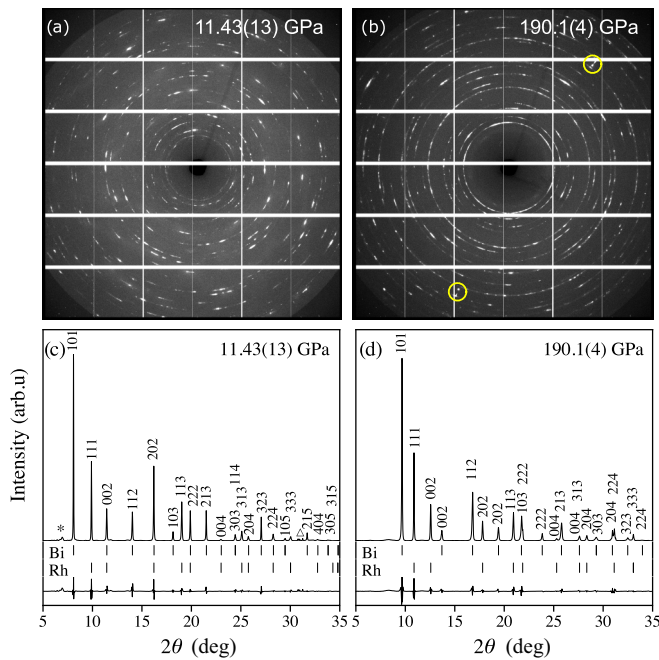


FIG. 2. 2D images [(a) and (b)], and integrated profiles with Le Bail fit residuals [(c) and (d)], from Rh in a Bi PTM at 11.4 and 190.1 GPa, respectively. The yellow circles in (b) identify Bragg reflections from the diamonds which were masked during the integration. The tick marks beneath the profiles in (c) and (d) show the calculated positions of the peaks from Rh and the Bi PTM and the residuals of the fits are shown below these. The asterisk at  $7^\circ$  in (c) indicates an impurity peak that was not observed at higher pressures and was therefore ignored. The triangle at  $31^\circ$  in (c) identifies weak peaks that arose from scattering from the pinhole upstream of the sample. These peaks did not move with pressure and were masked during the analysis process.

local pressure standard within the sample assembly during x-ray data collection. The Pt-Rh-Pt sandwich was then cut into circular disks of varying diameters using a laser drill. Gasket holes with initial diameters of 127 and 50  $\mu\text{m}$  for LH1 and LH2, respectively, and thicknesses of 28 and 14  $\mu\text{m}$ , were filled entirely with dried MgO powder to provide both chemical and thermal insulation from the diamonds. Each sample disk was then placed on top of the MgO powder and covered with a disk of precompressed MgO. The cell was then gently closed to tamp all the components into place. Finally, the cells were partially reopened to allow moisture to escape the sample chamber and subsequently dried in a vacuum oven at  $120^\circ\text{C}$  for 6 h before being closed once again [Fig. 1(b)]. The thicknesses of the MgO insulating layers above and below the Rh sample were approximately 10 and 3  $\mu\text{m}$  for LH1 and LH2, respectively.

## 2. XRD data collection and double-sided laser heating

The high-temperature XRD patterns from cells LH1 and LH2 were collected at the P02.2 Extreme Conditions Beamline (ECB) at the PETRA III synchrotron in Hamburg, Germany [16]. 2D XRD images were collected on a Perkin-Elmer area detector using an x-ray wavelength of 0.2917  $\text{\AA}$  and a beam size (FWHM) of  $2 \times 2 \mu\text{m}^2$ . The

DACs were mounted in a water-cooled copper block located approximately 395 mm from the detector. The precise sample-detector distance and detector tilts were again determined using a  $\text{CeO}_2$  standard and optimization in DIOPTAS [15]. Samples were optically heated using an on-axis, double-sided, continuous wave (1072 nm), heating system developed at the ECB [16] and the temperature was inferred from pyrometry measurements. To minimize the carbon diffusion and carbide contamination commonly observed in laser heating experiments on transition metals [17,18], the heating system was operated in a flash heating mode whereby the timing of the laser, x-ray shutters, and spectrometer data collection were all precisely controlled by an electronic triggering system. In this way, the time spent heating the sample was minimized with the heating duration governed by the minimum exposure time required to obtain the diffraction data. The laser heating time was 3.1 s and the x-ray collection time was 2.9 s. The combination of short x-ray wavelength and wide pressure cell opening angle provided sufficient access in reciprocal space for observation of up to 14–16 Bragg reflections for Rh and Pt depending on the pressure. However, analysis was typically based on a subset of reflections due to sample texture, peak overlap, and low intensity of some reflections.

## C. Data processing

The 2D diffraction images were integrated using the DIOPTAS analysis suite [15]. An additional third-order polynomial correction was applied to the  $2\theta$  values of all integrated patterns to ensure the differences between the ideal and observed  $\text{CeO}_2$  peak positions were minimized. The maximal correction necessary was less than  $0.001^\circ$  demonstrating the quality of the DIOPTAS calibration.

The 298-K isotherm parameters and cross correlations in Table I were determined via weighted least-squares minimization of the compression data in the Supplemental Material, Table S1 [19], using the EOSFIT7 suite [20]. The data summarized in Table S1 [19] were generated by fitting to the measured peak positions in 3900 diffraction profiles collected through grid scans of the sample area. Determination of the peak positions was performed using the batch fit software developed at DESY by Karnevskiy.

For the high-temperature patterns, Le Bail fits were performed on the integrated 1D profiles using JANA2006 [21]. The sample temperature was estimated using the average of the measured upstream and downstream pyrometry measurements. In the instances where only one temperature reading was recorded, the reading was assumed to be equivalent to the sample temperature. Temperature uncertainties were estimated to be  $\pm 10\%$  of the measured temperature, comparable to the uncertainties reported in previous experiments using the laser heating setup [16].

## III. RESULTS

### A. Room-temperature isothermal compression

Data were collected from two samples (RT1 and RT2) to a maximum pressure of 191 GPa at 298 K. The experimentally determined lattice parameters and volumes as a function of pressure for Rh are summarized in Table S1 [19]. The

TABLE I. The parameters, covariances ( $\sigma_{i,j}^2$ ), and weighted  $\chi^2$  for the best-fitting AP1, AP2, Vinet, and Birch-Murnaghan (B-M) EoSs to the ambient isothermal compression data of Table S1 [19]. Values in bold were fixed when fitting. The dagger ( $\dagger$ ) indicates an implied value.

EoS model	$V_0$	$K_0$	$K'$	$\sigma_{V_0 K_0}^2$	$\sigma_{V_0 K'}^2$	$\sigma_{K_0 K'}^2$	$\chi^2$
AP2	13.739(8)	268(4)	5.11(12)	-0.026	0.0006	-0.479	0.79
AP1	<b>13.764(2)</b>	266.7(7)	5.03 $\dagger$	0	0	0	1.27
AP2	<b>13.764(2)</b>	258(3)	5.36(9)	0	0	-0.228	0.99
Vinet	<b>13.764(2)</b>	257(2)	5.44(8)	0	0	-0.177	0.96
B-M	<b>13.764(2)</b>	261(3)	5.11(8)	0	0	-0.2	1.1
B-M	<b>13.764(2)</b>	<b>262.5</b>	5.05(2)	0	0	0	1.1

use of Bi as a PTM effectively mitigates issues with large nonhydrostatic stresses that can arise in compressing materials such as Rh, which possess relatively large yield strengths, to multimegabar pressures [13,22,23]. These nonhydrostatic stresses cause diffraction peak broadening and  $hkl$ -dependent peak shifts. The absence of these effects is demonstrated in Fig. 2 which shows 2D diffraction images [Figs. 2(a) and 2(b)] from pressure cell RT2 at 11.4 and 190.1 GPa, respectively, the resulting integrated profiles [Figs. 2(c) and 2(d)], and the residuals of Le Bail fits to these patterns. The integrated profiles display no obvious increases in peak widths, and the quality of the Le Bail fits is consistent indicating the absence of large  $hkl$ -dependent shifts, despite the large pressure difference.

### B. Local stress state of Rh in a Bi medium

As we wish to establish an accurate EoS for Rh, and as the measured compressibility of a material can be affected by the nonhydrostaticity of the pressure environment, we quantified the local stress state in detail in both the Rh samples and Bi PTM at various pressures by determining the uniaxial stress component ( $t$ ) using the peak-shift analysis method of Singh [24–26], the details of which are given in the Supplemental Material [19, Sec. IV]. In both materials,  $t$  was determined using up to 9 Bragg reflections but no less than 5. Rather than simply making a single average measurement of  $t$  in the Rh at each pressure, we exploited the submicron beam size and fast-scanning abilities of beamline ID27 to map  $t$  across both the Bi PTM and Rh sample from 2D grid scans.

Figure 3(a) shows the size and location of the gasket hole relative to the 100- $\mu\text{m}$  diamond culet at 189 GPa, as determined from a grid scan. Figure 3(c) shows the variation of  $t$  across the  $22 \times 22 \mu\text{m}^2$  area of the Bi PTM at 110 GPa that contains the  $10 \times 10 \mu\text{m}^2$  Rh sample, while Fig. 3(d) shows the variation of  $t$  within the Rh sample at the same pressure. The maximal  $t$  values within the Bi are  $\pm 0.5$  GPa, emphasizing its excellence as a PTM, while the  $t$  values within the Rh, with its much higher yield strength, ranged between  $\pm 4$  GPa. However, volumes of the Rh separated by only  $1 \mu\text{m}$  showed quite large and nonphysical differences in  $t$ , while the values of  $t$  in the Rh and the Bi PTM measured at the same location, and therefore from the same diffraction profile, showed no correlation [Fig. 3(b)], suggesting that there is significant noise in the  $t$  measurements. The average value of  $t$  in the Rh sample at 110 GPa is  $1.0(15)$  GPa, where the uncertainty is the standard deviation.

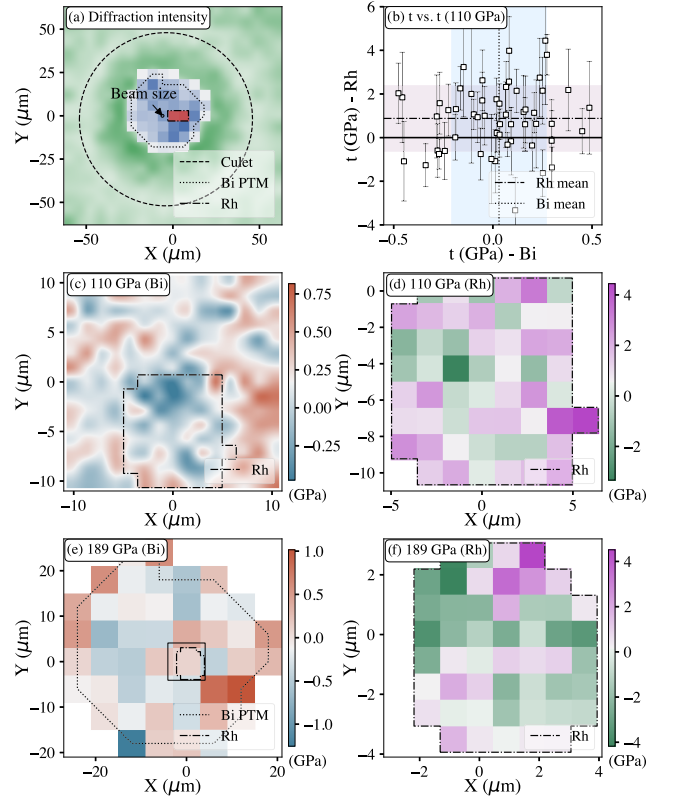


FIG. 3. (a) Grid scan of the 100- $\mu\text{m}$  diamond culet at 189 GPa, showing the size and location of the gasket hole, as determined by the presence of scattering from the Bi PTM. The relative size of the x-ray beam is shown for comparison. (b) A plot of  $t$ -Rh versus  $t$ -Bi, as measured at the same 55  $X$ - $Y$  positions in (c) and (d). There is no correlation between the values of  $t$  in the Rh and the Bi surrounding it. The vertical dotted and horizontal dashed-dotted lines represent the average  $t$  values of the Bi and Rh, respectively while the shaded blue and red areas define the extent of one standard deviation. We found 55% of the Bi data points and 51% of the Rh data points were within one error bar of zero. (c) A map of the uniaxial stress component ( $t$ ) in the Bi PTM at  $\sim 110$  GPa calculated under the assumption  $\alpha = 1$ . The location of the Rh sample is shown by the black dashed-dotted line. (d) The corresponding  $t$  map for the  $10 \times 10 \mu\text{m}^2$  Rh sample at the same pressure. Note the nonphysical changes in  $t$  on  $\mu\text{m}$  length scales. (e) A  $t$  map across the Bi at 189 GPa. The extrema in the  $t$  values are comparable to those measured at 110 GPa. The location of the Rh is shown with a dotted-dashed line. (f) A high-resolution  $t$  map ( $9 \times 9$  grid with  $0.875\text{-}\mu\text{m}$  steps) of the Rh at the same pressure, again showing nonphysical changes in  $t$  on  $\mu\text{m}$  length scales.

TABLE II. The as-published EoS parameters for Rh [5–7], Ru [36], and Pd [7,37], and the revised parameters obtained by fitting AP2 model parameters used in the data linearization. Numbers given in bold were held fixed during the refinement. The asterisk denotes averaged from two experimental measurements and fixed during refinement.

Material	Model	Published			Refitted AP2		
		$V_0$ ( $\text{\AA}^3$ )	$K_0$ (GPa)	$K'$	$V_0$ ( $\text{\AA}^3$ )	$K_0$ (GPa)	$K'$
Rh [6]	B-M	13.738	270.0	4.756	13.7455(5)	266.2(2)	4.939(4)
Rh [5]	B-M	13.73(7)	301(9)	3.1(2)	13.714(14)	308(8)	2.8(3)
Rh [7]	B-M	13.762(16)	244.0(66)	5.11(24)	13.757(14)	246.5(61)	5.05(24)
Ru [36]	B-M	13.561(3)	323.4(11)	4.2(2)	<b>13.5889*</b>	320.4(6)	4.25(2)
Pd [37]		14.603					
Pd [7]	Vinet	14.645(18)	189.3(30)	5.473(63)	14.7258(2)	179.6(2)	5.620(8)

Figure 3(e) shows a low-resolution (6- $\mu\text{m}$  steps)  $t$  map of the Bi PTM across the full sample chamber at 189 GPa, the highest pressure at which such maps were made, while Fig. 3(f) shows a high-resolution (0.875- $\mu\text{m}$  steps)  $t$  map across the  $8 \times 6 \mu\text{m}^2$  Rh sample at the same pressure. The data exhibit the same noisy behavior seen at 110 GPa, with maximal  $t$  values of  $\pm 1.25$  GPa in the Bi,  $\pm 4.5$  GPa in the Rh, and average values of 0.1(4) GPa and  $-0.5(1.9)$  GPa, respectively.

While the measured values of  $t$  can be used to calculate the hydrostatic lattice parameters  $a_p$  (see Supplemental Material [19, Sec. IV]), from the measured lattice parameters  $a_m$ , the large uncertainties and scatter in  $t$  increases the scatter in  $a_p$  relative to  $a_m$ , rather than reducing it, as would be expected if correcting for nonzero values of  $t$ . As a result, we have followed the approach of Takemura *et al.* [27] in their construction of a hydrostatic EoS for gold, in which they used only the (111) peak from Au to determine the pressure because, for fcc structures, the (111) reflection is least affected by nonhydrostatic compression. Similarly, for a body-centered-cubic (bcc) structure like Bi-V, it is the (222) reflection that is least affected by nonhydrostaticity, and thus the pressures in this work have been calculated primarily using the measured position of the (222) peak in Bi-V and the associated unit-cell volume of Rh was determined from the position of the (111) peak.

### C. Ambient temperature EoS

The compression data to 191 GPa are shown in Table S1 [19] and are plotted in Fig. 4. We have analyzed the data using Holzapfel's second-order adapted polynomial of order L (AP2) EoS [28]:

$$P(x) = 3K_0 \frac{(1-x)}{x^5} e^{c_0(1-x)} [1 + xc_2(1-x)], \quad (1)$$

where  $K_0$  is the zero-pressure bulk modulus,  $K'$  is its pressure derivative,  $x = (V/V_0)^{1/3}$ ,  $c_0 = -\ln(3K_0/P_{\text{FG0}})$ ,  $c_2 = (3/2)(K' - 3) - c_0$ ,  $P_{\text{FG0}} = a_{\text{FG0}}(nZ/V_0)^{(5/3)}$  is the Fermi-gas pressure,  $Z$  is the atomic number,  $a_{\text{FG0}} = 2337 \text{ GPa } \text{\AA}^5$  is a constant, and  $n$  is the number of atoms in a chemical formula. Fitting this EoS to our data using EOSFIT7 [20] gave the results and parameter cross correlations listed in Table I, along with the optimized parameters from an AP1 ( $c_2 = 0$ ), a second-order Vinet, and a third-order Birch-Murnaghan (B-M) fit to the same data. The AP2 fit to the data is plotted

in Fig. 4 alongside experimental and theoretical data from previous studies. Formulas for error and parameter correlation propagation through the AP2 formalism are provided in the Supplemental Material [19, Sec. VII]. The room-temperature compression curve for Rh from this study agrees very well with the static compression measurements of Young *et al.* from 31 to 83 GPa [6], and to higher pressures, as indicated by the extrapolated AP2 fit (parameters in Table II) to their data. However, the  $V_0$  as determined through extrapolation of their B-M fit is slightly smaller than our experimentally measured value of 13.764(2)  $\text{\AA}^3/\text{atom}$  and explains their moderately larger and smaller values for  $K_0$  and  $K'$ , respectively, due to correlation between the fitting parameters. Our data agree less

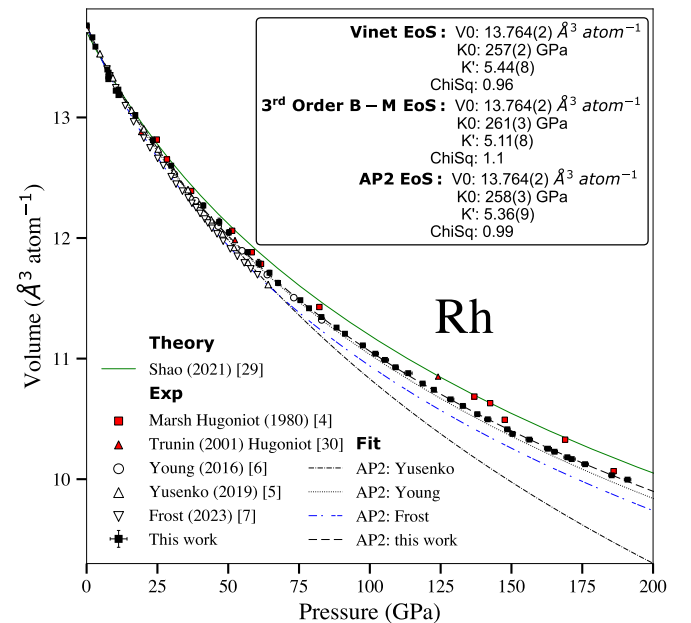


FIG. 4. The atomic volume of Rh as a function of pressure along the 298-K isotherm. Experimental data from this study (■) are shown and the dashed line through them is the best second-order APL fit. Experimental data from the previous studies of Yusenko *et al.* [5] ( $\Delta$ ) and Frost *et al.* [7] ( $\nabla$ ) are also shown, along with pseudo-data points ( $\circ$ ) generated at regularly spaced intervals using the Rh EoS of Young *et al.* [6]. Second-order APL fits to these data are also shown, along with the compressibility calculated by Shao *et al.* [29], and the shock compression data for Rh along the principal Hugoniot measured by Marsh *et al.* [4] and Trunin [30].

well with the previous static compression study of Yusenko *et al.* [5] to 64 GPa showing volumetric ( $V/V_0$ ) deviations of  $\sim 0.5\%$  by 64 GPa. An AP2 fit to their data extrapolated up to 2 Mbar diverges significantly from our results as shown in Fig. 4. Interestingly, we find our ambient volume measurement and  $K'$  value, as determined through refinement of the B-M EoS, to agree well with the compressibility behavior observed by Frost *et al.* [7] up to 60 GPa. However, their value for  $K_0$  [244.0(66) GPa] is  $\sim 6.5\%$  less than ours [261(3) GPa] (see Tables I and II).

While  $K_0$  in Table I was obtained from fitting to the ambient isothermal compression data, its value can also be determined from ultrasonic studies of elastic constants. For example, Walker *et al.* [31] investigated the elastic moduli of Rh between 4.2 and 293 K and determined  $C_{11}$ ,  $C_{12}$ , and  $C_{44}$  values of 412.6, 193.5, and 184.1 GPa, respectively, at 293 K. Using the definition of the isentropic bulk modulus for a cubic system [32]

$$K_s = \frac{1}{3}(C_{11} + 2C_{12}), \quad (2)$$

these measurements give  $K_s = 266.53$  GPa for Rh. Through standard thermodynamic identities,  $K_s$  is related to the isothermal bulk modulus ( $K_T$ )

$$K_T = K_s \left[ 1 + \frac{\alpha^2 V T K_s}{C_p} \right]^{-1}, \quad (3)$$

where  $\alpha$  is the volumetric thermal expansion and  $C_p$  is the specific-heat capacity at constant pressure. Using  $\alpha = 2.4283 \times 10^{-5}$  [33],  $V_0 = 13.764 \text{ \AA}^3/\text{atom}$  ( $8.055 \times 10^{-5} \text{ m}^3/\text{kg}$ ),  $C_p = 241.58 \text{ J/kg K}$  [34], and  $T = 293 \text{ K}$ , we find  $K_T = 262.5$  GPa, in excellent agreement with the values obtained by fitting to our compression data (Table I) to within experimental uncertainty.

To better constrain the pressure derivative of the bulk modulus ( $K'$ ), we have also refined the B-M EoS using fixed values of  $V_0$  and  $K_0$ . The refinement results are given in the final line of Table I. We observed negligible change in the quality of the fit upon reducing the number of refinable parameters and the change in the value of  $K'$  was within the associated uncertainty.

#### D. EoS behavior under strong compression

If the EoS of Rh is to be used in extrapolations above 191 GPa then one needs to have confidence that it shows no evidence of anomalies. It is then informative to inspect the compression behavior using the linearization scheme outlined by Holzzapfel [35] where the  $x$  axis ( $\sigma$ ) corresponds to the volume-scaled Thomas-Fermi radius ( $\sigma = \sigma_0 x$ ) with  $x = (V/V_0)^{1/3}$  and  $\sigma_0 = [3ZV_0/(4\pi)]^{1/3}$ , and the  $y$  axis is given by  $\eta_{\text{APL}} = \ln\{P x^5/[P_{\text{FG}}(1-x)]\}$  where  $P_{\text{FG}}$  is the Fermi gas pressure, as above. In  $\eta_{\text{APL}}-\sigma$  space, changes in material compressibility are exaggerated, and the first-order APL EoS (AP1) with  $c_2 = 0$  is represented by a straight line passing through the origin. In previous work, the compressive behavior of materials has generally been classified into four categories (ideal, simple, regular, and irregular [28]) which are easily identified in the linearized space. Materials exhibiting ‘‘ideal’’ compression follow a straight line with gradient  $d\eta/d\sigma = -0.567 \text{ \AA}^{-1}$ .

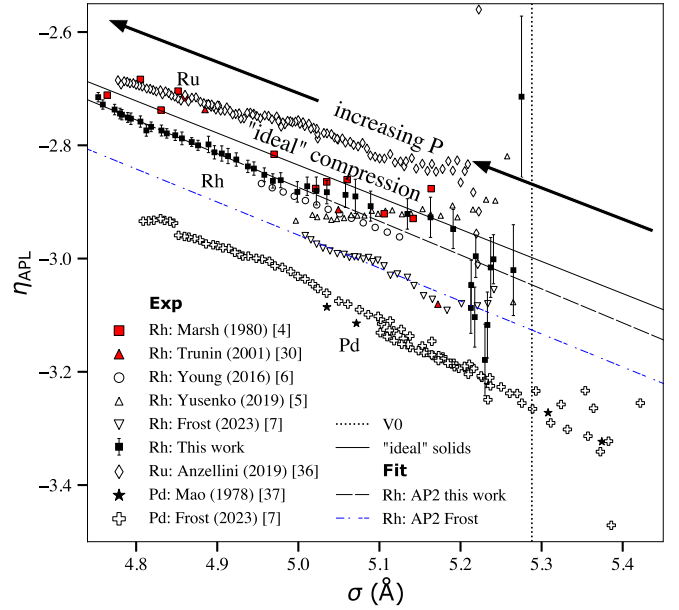


FIG. 5. Linearization of the compression of Rh shown in the form of an  $\eta_{\text{APL}}-\sigma$  plot. In this space, pressure increases from right to left and materials that are well represented by a first-order APL EoS will follow a linear trend. Ideal compression (see text for details) is shown by the solid black line and the dotted vertical line shows the location of  $V_0$  for Rh. The data from this study on Rh (■) are shown, alongside the previous Rh data [5–7], as well as comparative data from Ru [36] and Pd [7,37]. Also displayed for comparison are the linearized shock data of Marsh *et al.* [4] and Trunin [30].

The linearized 298-K compression data of this study are plotted in Fig. 5 alongside the Rh experimental data of Yusenko *et al.* [5], Frost *et al.* [7], and experimental data for Ru [36], and Pd [7,37] for comparison. Also plotted are representative data points generated from the Birch-Murnaghan Rh EoS of Young *et al.* [6] and the shock data of Marsh *et al.* [4] and Trunin [30]. For consistency, we have refitted this literature data using an AP2 EoS to determine  $V_0$ . The refinement parameters are given in Table II. Close to  $\sigma_0$ , indicated by the vertical dashed line in Fig. 5, the linearization scheme is extremely sensitive to small differences between the measured  $V$  and the fixed  $V_0$ . As a result, increased scatter and larger uncertainties are observed near  $\sigma_0$ . At higher pressures (smaller  $\sigma$ ) we find the current data follow a linear trend (almost parallel to ‘‘ideal’’ compression) up to the highest measured pressures of 191 GPa. The AP1 fit for Rh (Table I) yields a gradient ( $d\eta/d\sigma = -0.576 \text{ \AA}^{-1}$ ) very close to ‘‘ideal.’’ However, moderate improvement in the fit was achieved using the AP2 model which relaxes the value of  $c_2$ , thus, increasing the number of fitting parameters and allowing for slight curvature in the  $\eta-\sigma$  space. A material’s compression can be considered ‘‘regular’’ as long as  $c_2$  in Eq. (1) remains relatively small, such that  $|c_2 - (c_0 - c_{0,\text{ideal}})| < 0.5$  where  $c_{0,\text{ideal}} = -\beta_{\text{ideal}}\sigma_0$ , and  $\beta_{\text{ideal}} = 0.567 \text{ \AA}^{-1}$  represents an average slope for all regular elements [28]. From the best-fitting AP2 values with refined  $V_0$ ,  $K_0$ , and  $K'$  in Table I,  $c_0 = 3.04$  and  $c_2 = 0.12$ , and hence  $|c_2 - (c_0 - c_{0,\text{ideal}})| = 0.073$ . As this value is  $\ll 0.5$ , Rh falls definitively within the category of ‘‘regular’’ solids over the pressure range studied. The linearized data of this study show

good agreement with those of Young *et al.* [6], collected from 31 to 83 GPa using a Ne pressure medium, although there is a small offset in  $\eta$  between the two. By contrast, the linearized data of Yusenko *et al.* [5] display very different linearized behavior, with an unusual positive gradient and without the correct limiting behavior of  $\lim_{\sigma \rightarrow 0} \eta(\sigma) = 0$ . The positive gradient in the linearization plot suggests that the compressibility is unusually high, as is also evident in Fig. 4, but the reasons for this are unclear.

The linearized Rh data of Frost *et al.*, while having the same gradient as the current study, have a more significant offset of  $\sim 0.1$  in  $\eta$ . Offsets in  $\eta$  might be explained by the use of different pressure gauges, differences between the local pressure at the pressure gauge and the sample, or small differences in  $V_0$  as the linearization scheme is sensitive to this choice. Converting the pressures of Frost *et al.* to make them consistent with the calibration used in this study changed the pressures by only 0.1 GPa at 60 GPa, much smaller than the  $\sim 5$ -GPa difference observed (see Fig. 4). For the pressure conversion, the experimental data of Dewaele *et al.* [38] were used to identify the atomic volume of copper associated with the atomic volume of W as measured by Frost. The pressure was then calculated from the Cu volume using the EoS of Fratanduono *et al.* [39] previously applied to calibrate the Bi EoS used in this study [13]. However, the images shown by Frost *et al.* of their Rh loading show a significant separation ( $\sim 35 \mu\text{m}$ ) between the sample and the W calibrant before compression. While the separation was probably smaller at higher pressures, pressure gradients within the sample chamber may have resulted in the sample and calibrant being at different pressures. An advantage of using Bi as both the PTM and pressure calibrant is that diffraction data are always obtained simultaneously, even when using a submicron x-ray beam.

Over the range of  $\sigma$  in Fig. 5, the compressive behavior of Rh, and its neighboring transition metals in the periodic table (Ru and Pd), follow a relatively linear trend. Such behavior is in contrast to materials like Rb [40], Y [41], and Sm [42] which undergo several phase transitions manifesting as nonlinearity in the  $\eta$ - $\sigma$  space before finally exhibiting “regular” compression at high pressure. As Rh exhibits “regular” compression throughout the full pressure range studied, pressure-induced phase transitions are unlikely and extrapolation of the AP2 fit beyond the experimental data should provide an accurate representation of the material response.

### E. $P$ - $V$ - $T$ data and a Rh thermal EoS

Using the double-sided flash laser heating system at the Petra-III Extreme Conditions Beamline (ECB), and described in detail in Konopkova *et al.* [16], we collected  $P$ - $V$  data at elevated temperatures for Rh at pressures from 5–148 GPa and temperatures between 298–2700 K. The *in situ* pressure was determined from the unit-cell volume of the  $0.9 \mu\text{m}$  Pt coatings on the surfaces of the Rh foil sample and the Pt thermal EoS of Sokolova *et al.* [43,44]. The  $P$ - $V$ - $T$  data are provided in Tables S2 and S3 in the Supplemental Material [19]. Before each heating run, a diffraction image was collected to obtain the unit-cell lattice parameters of Rh and Pt at 298 K ( $a_{0,298}$ ), from which two “cold” pressures ( $P_{298}$ ) were

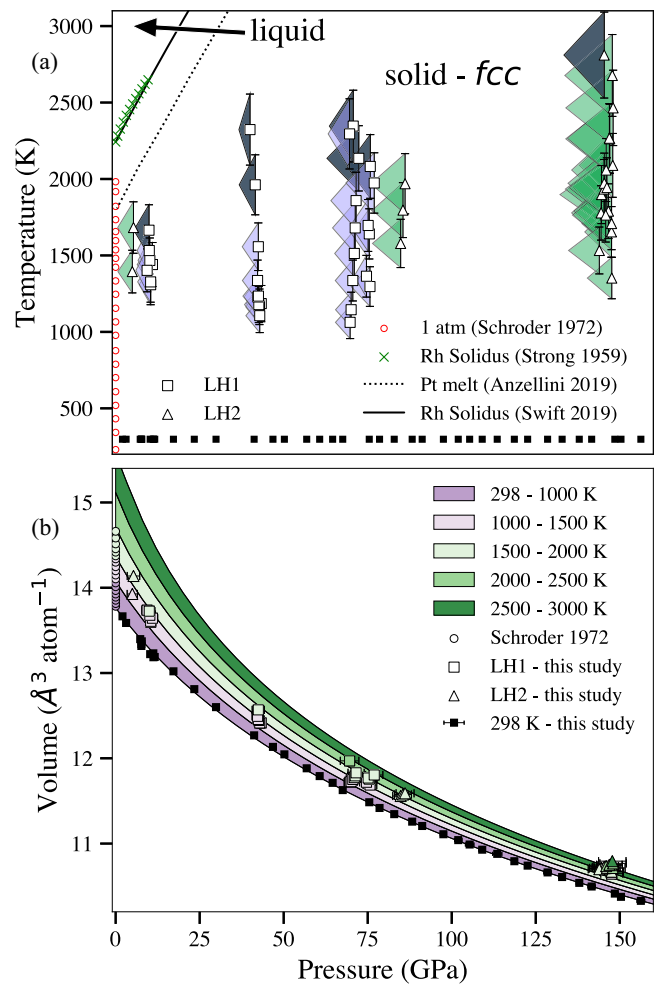


FIG. 6. The high-pressure and temperature data points collected from laser heating on Rh and used in the determination of the thermal EoS. (a) Data in pressure-temperature space. The solid black line marks the Rh melt boundary calculated by Swift *et al.* [9] and the green crosses show the experimentally determined melt cure of Strong *et al.* [45]. For comparison, the dotted black line denotes the solid-liquid phase boundary of platinum [46]. The solid black squares represent the 298-K isothermal compression data of this study and the open red circles are the isobaric data of Schroder *et al.* [47]. The open black squares and triangles represent the laser heating data from LH1 and LH2, respectively, from this study while the purple and green polygons denote the thermal pressure and the temperature uncertainty in each data point. The left side of the polygon is determined from the Pt pressure measured before the heating run at 298 K while the right side is determined from the *in situ* Pt volume measured under heating conditions. The data points with gray polygons exhibited textural changes in the postheating pattern and were excluded from the thermal EoS refinement. (b) Data in pressure-volume space. Here isotherms generated using the refined thermal model for 298, 1000, 1500, 2000, 2500, and 3000 K (see Table S5 in the Supplemental Material [19]) are plotted alongside the experimental data. The data points are colored based on the measured sample temperature and the intervals indicated.

calculated using their ambient temperature equations of state. High-temperature diffraction images were then collected at the same sample position with typical heating and x-ray exposure times of  $\sim 3$  s. The cold pressures for the Rh and

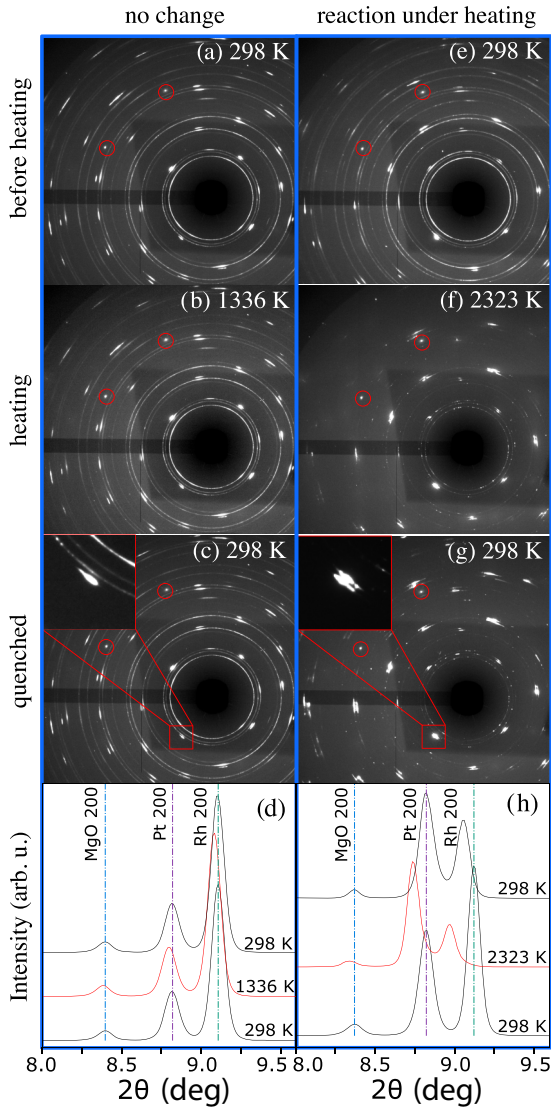


FIG. 7. Diffraction images and profiles from two heating and cooling cycles. (a)–(c) Show the diffraction images obtained before, during, and after heating in the first cycle where the maximum temperature inferred from pyrometry was  $1336 \pm 134$  K. No obvious indications of reaction products are present in the quenched image. (d) Shows the corresponding integrated 1D profiles over a limited  $2\theta$  range in which the peaks in the high- $T$  profile (red) are shifted to lower  $2\theta$  values and the quenched pattern matches the profile obtained before heating. In contrast, clear changes in the 2D images are observable in images (e)–(g) which show the stages for the second heating cycle reaching a maximum temperature of  $2323 \pm 232$  K. The enlarged region in (g) highlights the increased intensity between the (200) Bragg reflections for Rh and Pt in the quenched image. (h) Shows the integrated profiles from images (e)–(g), highlighting the differences in the before and after profiles. In particular, (h) shows that the (200) peaks from the MgO and Pt return to their initial, preheating, positions while the Rh (200) peak remains displaced to lower  $2\theta$  after cooling, indicating an expanded lattice. Since the peaks from both the MgO and Pt suggest that the pressure in the cell returned to its starting value after heating, the expanded Rh lattice likely indicates the inclusion of Pt within the Rh lattice. In the 2D images, Bragg reflections from the diamond anvils have been indicated with red circles.

Pt prior to heating differed by as much as 9 GPa at  $\sim 130$  GPa (see Table S3 [19]). This is likely due to anisotropy of the local stress state in the cell as MgO is not a particularly good pressure-transmitting medium. Although there is thus uncertainty in the initial pressures at 298 K, at high temperatures the differential stress effects in the DAC typically relax as the sample's capacity to support shear gradients decreases with increasing temperature. To ensure consistency with the thermal pressures determined at high temperatures, we used the cold pressure values measured from the Pt in our calculations.

After heating, the sample was allowed to cool to 298 K before a postheating diffraction pattern was collected. In the absence of any changes in the 2D diffraction pattern, such as those displayed in Figs. 7(e) or 7(f) and discussed later, or the appearance of new peaks, a new heating run was performed at the same sample position. The postheating diffraction profile then doubled as the preheating data collection for the next run. Heating runs in which changes in the postheating diffraction images were observed are indicated with a degree symbol in Table S2 [19]. After these heating runs the sample was moved with respect to the x-ray beam to a new position, indicated by the asterisks (\*) in Table S2 [19], and the high-temperature data from the previous heating run were not included in the refinement of the thermal model. The data points in Table S2 [19] are graphed in Fig. 6(a).

By combining the ambient pressure thermal expansion data of Schroder *et al.* [47], the 298-K isothermal compression data, and the high-pressure-temperature laser heating data of this study, we have constructed a thermal EoS for Rh from 0–191 GPa and 300–2700 K. The EoS model is a two-component pressure model with a volume-dependent isothermal reference part  $P(V, T_{\text{ref}})$ , and a temperature-dependent thermal pressure part  $P_{\text{th}}(T)$ :

$$P(V, T) = P(V, T_{\text{ref}}) + P_{\text{th}}(T). \quad (4)$$

The isothermal reference term is simply the AP2 reference isotherm with parameters given in Table I while the thermal pressure is of the single Einstein temperature form suggested by Holland and Powell [48]:

$$P_{\text{th}}(T) = \alpha_0 K_0 \left( \frac{\theta_E}{\xi_0} \right) \left( \frac{1}{\exp(\theta_E/T) - 1} - \frac{1}{\exp(\theta_E/T_{\text{ref}}) - 1} \right), \quad (5)$$

where  $\alpha_0$  is the ambient volumetric thermal expansion coefficient,  $\theta_E$  is the Einstein temperature, and  $K_0$  is the ambient isothermal bulk modulus. The parameter  $\xi_0$  is introduced in the thermal expansion model of Kroll *et al.* [49] and is given by

$$\xi_0 = \frac{(\theta_E/T_{\text{ref}})^2 \exp(\theta_E/T_{\text{ref}})}{[\exp(\theta_E/T_{\text{ref}}) - 1]^2}. \quad (6)$$

This thermal model is implemented in the framework of EOSFIT7C [20,50] and, as highlighted by Angel *et al.*, it benefits from the product  $\alpha K_T$  reducing to zero at low temperatures while also limiting to a constant value at high  $T$ . By extension, this behavior corresponds to approximately linear temperature-dependent behavior of the bulk modulus



TABLE III. The optimized AP2-Holland-Powell thermal EoS parameters for Rh to 191 GPa and 2700 K, along with the optimized parameters for use in DIOPTAS [15]. The numbers shown in bold were fixed during the refinements. Uncertainties on  $V_0$ ,  $K_0$ , and  $K'$  are equivalent to those given in Table I. The uncertainty on  $V_0$  was derived from the experiment while the uncertainties on  $K_0$  and  $K'$  were determined through least-squares refinement to the 298-K isothermal data with fixed  $V_0$ . The uncertainties on  $\alpha_0$  and  $\theta_E$  for the AP2-HP model were calculated using EOSFIT7C.

Model	AP2-HP	DIOPTAS
$V_0$ ( $\text{\AA}^3$ )	<b>13.764</b>	<b>13.764</b>
$K_0$ (GPa)	<b>257.536</b>	<b>260.54</b>
$K'$	<b>5.3578</b>	<b>5.114</b>
$\alpha_0$ (1/K) [ $\times 10^{-5}$ ]	2.050(12)	2.99
$\theta_E$ (K)	779(5)	n/a
$dK_0/dT$ (GPa/K) [ $\times 10^{-5}$ ]	n/a	-6.43
$d\alpha/dT$ (K $^{-2}$ ) [ $\times 10^{-9}$ ]	n/a	1.27
$dK'/dT$ (1/K) [ $\times 10^{-10}$ ]	n/a	-9.3

and thermal expansion coefficient above  $\theta_E$  while they both limit to constant values at low temperatures.

We used EOSFIT7C to perform the thermal parameter refinements using weighted least-squares minimization. In the isobaric expansion data, we assumed a pressure uncertainty of  $\pm 0.05$  bar and a volume uncertainty of  $\pm 0.001$   $\text{\AA}^3/\text{cell}$ . We also held the isothermal AP2 parameters fixed when performing the refinements. The optimized model parameters are given in Table III. For comparison, several isotherms generated from the fitted thermal model are plotted alongside the high-pressure-temperature data in Fig. 6(b) and the  $P$ - $V$  data points for these isotherms are provided Table S5 [19]. This simple two-parameter thermal pressure model captures both the ambient pressure isobaric expansion behavior and the laser heating data up to  $\sim 100$  GPa. At higher pressures, the discrepancy between the thermal model and experimental data is greatest and, consequently, the model refinement is least constrained by these points. A thermal model with a greater number of refinable parameters could be optimized in place of the Holland-Powell (HP) model to capture this behavior but we believe more data in this regime is required before this is justified and therefore the HP thermal model is appropriate for the current data set.

As we wish to use Rh as a  $P$ - $T$  gauge in future XFEL experiments, we also developed a thermal EoS model suitable for use in the widely used 2D x-ray diffraction integration software, DIOPTAS [15]. Using the refined AP2-HP thermal model, we generated a grid of  $P$ - $V$ - $T$  data points [at temperatures of 298, 1000, 1500, 2000, 2500, and 3000 K, between 0–200 GPa in 0.5-GPa increments (see an abridged Table S5 [19])] and then used the optimization approach described in McHardy *et al.* [51] to generate a Rh jcpds parameter file for use in DIOPTAS. The optimized parameters for this file are given in Table III, and replicate the pressures calculated by the AP2-HP EoS to within  $\pm 0.55$  GPa over the full  $P$ - $V$ - $T$  grid. The reparametrized DIOPTAS EoS also reproduces the experimental data to within a maximum deviation of  $\Delta V = 1.2\%$  at  $\sim 148$  GPa and  $\sim 2700$  K.

## F. Pt-Rh high-temperature alloying

As stated previously, we conducted repeated heating studies at a specific sample location until we observed changes in the postheating 2D diffraction images or integrated profiles. At that point, we moved to a new sample location before continuing the experiment. An example of the changes seen is illustrated in Fig. 7, which shows the behavior observed in a sample when heated to 1336 K and then cooled [Figs. 7(a)–7(c)] and then heated to 2323 K and then cooled [Figs. 7(e)–7(g)]. On cooling from 1336 K, the diffraction profile is the same as that obtained before heating [Fig. 7(d)]. However, after cooling from 2323 K, while the MgO and Pt (200) peaks return to their preheating positions, and hence indicate that the sample pressure is unchanged, the Rh (200) diffraction peak is displaced to lower  $2\theta$  than its initial position [Fig. 7(h)], suggesting an expanded lattice. This change in the relative spacing of the Pt and Rh peaks is also evident in the 2D image [Fig. 7(g)].

The expanded lattice parameter seen in the postheated Rh likely arises from the partial alloying of the sample with the hot Pt coating, resulting in the apparent expansion of the Rh. We can estimate the extent of the alloying using Vegard's law and the change in the measured lattice parameter of the Rh obtained from the before and after heating profiles in Fig. 7(h). The lattice parameters of the Pt and Rh prior to heating were 3.7930(3)  $\text{\AA}$  and 3.6687(3)  $\text{\AA}$ , while after heating the lattice parameter of the Rh had increased to 3.6973(3)  $\text{\AA}$ . Using Vegard's law

$$a_{\text{alloy}} = xa_{\text{Pt}} + (1-x)a_{\text{Rh}}, \quad (7)$$

where  $x$  is the fraction of the Pt alloyed with the Rh, and these lattice parameters give  $x = 0.24$ , and hence the alloy is  $\text{Rh}_{0.76}\text{Pt}_{0.24}$ . Given the initial starting thicknesses of the Rh (6.4  $\mu\text{m}$ ) and the Pt coatings (1.8  $\mu\text{m}$ ) and complete alloying of the Rh and the Pt, we would expect  $\text{Rh}_{0.78}\text{Pt}_{0.22}$ .

## G. Heating-cooling cycles in the LH DAC

Given the observed alloying at high temperatures, we made a more detailed study of the sample behavior as a result of repeated heating at the same sample location at 65 GPa. After collecting a preheating diffraction profile (heating cycle No. 0), 13 heating runs were then made at the same sample location, while the sample temperature was increased from  $\sim 1060$  K on cycle No. 1 to 2370 K on No. 13 [Fig. 8(a)]. As shown in Fig. 8(b), there was no change in the postheating diffraction profiles after the first five heating cycles, at which point the maximum temperature reached was 1580 K. A small shift of both the Pt and Rh diffraction peaks to slightly smaller values of  $2\theta$  showed that the pressure decreased slightly after each heating cycle [Fig. 8(e)] and that the pressure determined separately from the Rh and Pt was very similar [Fig. 8(e)].

Starting at heating cycle No. 6, however, we saw a change in the relative lattice parameters of the Rh and the Pt [Fig. 8(c)], clearly evident in the movement of the diffraction peaks, an increase in the apparent uniaxial stress component  $t$  [Fig. 8(d)], and a difference in the pressure experienced by the Rh and Pt [Fig. 8(e)], which was further increased after accounting for the different values of  $t$  in the Rh and Pt. All of these changes remained relatively unchanged until the

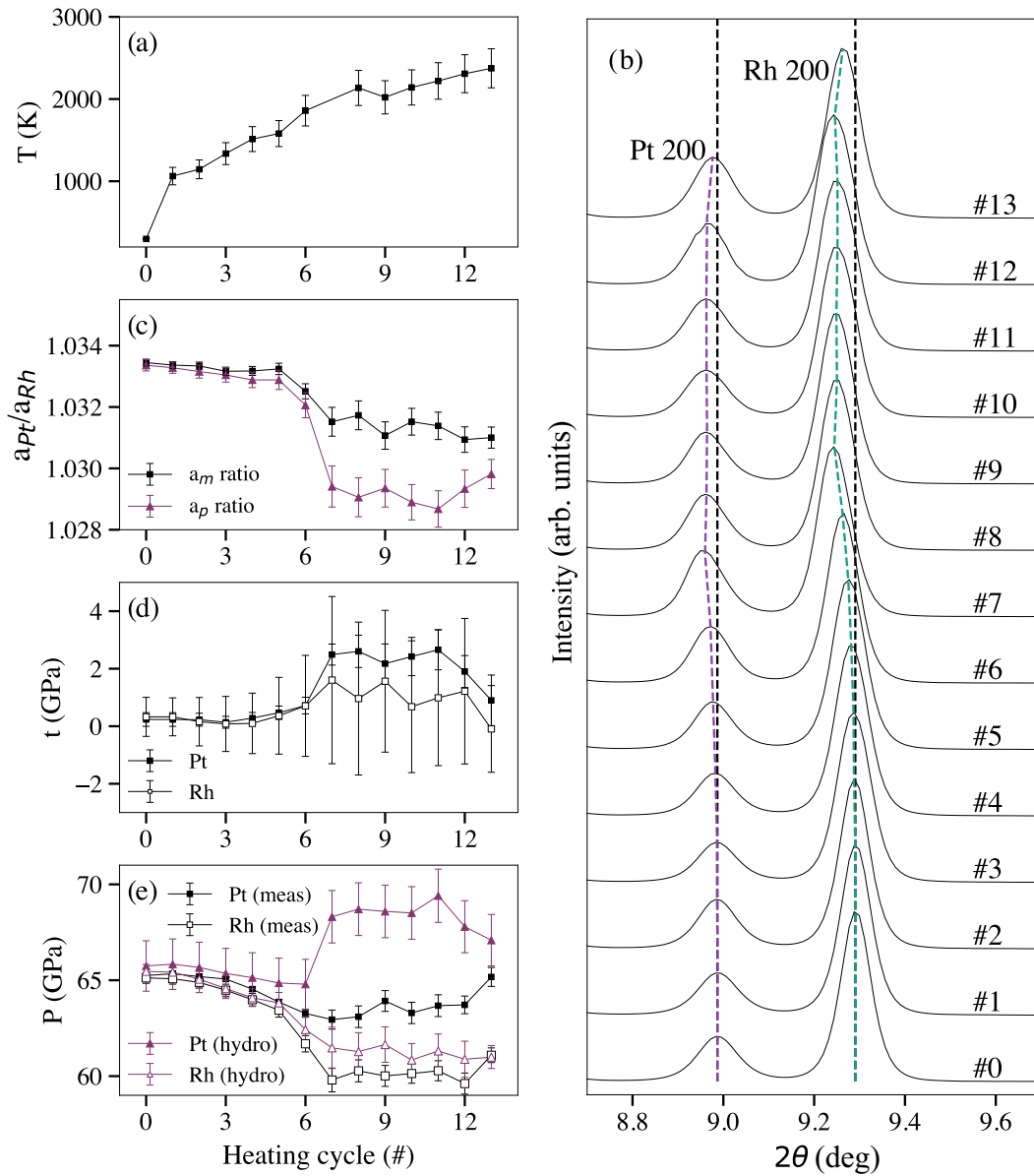


FIG. 8. The effects arising from repeated laser heating and cooling at the same sample location. Cycle No. 0 refers to the data collected prior to the first laser heating cycle. (a) The peak sample temperature reached in each heating cycle, as inferred from the pyrometry measurements. No pyrometry data were acquired for cycle No. 7 due to the saturation of the detector during this run. (b) The integrated profiles obtained from the quenched samples after each heating run, highlighting the (200) peaks from the Pt and Rh. The peaks from both materials show a shift to lower  $2\theta$  angles with increased heating cycles, typical of a pressure relaxation following repeated heating. (c) The ratio of the Pt and Rh unit-cell parameters after each heating cycle. The black squares show the as-measured data while the triangles denote the hydrostatically corrected ratio based on the measured  $t$  parameter. Both the measured and hydrostatic ratios remain relatively constant for the first six cycles, after which a reduction in the ratio likely indicates a reaction in the sample upon reaching some threshold temperature. (d) The  $t$  parameter for the Pt (■) and Rh (□) after each cycle. An increase in the  $t$  parameter is observed after the sixth heating cycle and is accompanied by a significant increase in the uncertainty. (e) The measured and corrected pressures in the Pt and Rh samples after heating. Both materials indicate a decrease in pressure in agreement with (b), however, the apparent pressure drop in the Rh is significantly greater. This difference is exaggerated in the corrected hydrostatic data.

final heating cycle (to 2370 K) where  $t$  decreased, and the pressure experienced by the Rh and Pt became more similar again. Due to the large uncertainties on the uniaxial stress component after heating cycle No. 6, it was not possible to determine whether the increase in  $t$  was related to changes in the local stress state or to the changes in the sample composition.

The results of this experiment suggest that while the data from heating cycles No. 1–No. 5 could be used in obtaining the thermal EoS of Rh, the higher-temperature data at this pressure could not. While studies as detailed as this were not conducted at other pressures, we did monitor the evolution in the lattice parameter ratio ( $a_{\text{Pt}}/a_{\text{Rh}}$ ) at other pressures as this provided a rapid means of deciding when to move to a

new sample position. As already mentioned, only spectra that did not exhibit such changes in the postheating 2D diffraction images or integrated profiles were used in the creation of the Rh thermal EoS.

#### IV. CONCLUSIONS

By combining room-temperature compression and laser heating studies, we have determined a thermal equation of state of Rh to 191 GPa and 2700 K. By exploiting Bi's excellence as a PTM, we have quasihydrostatically compressed Rh to 191 GPa at 300 K, and have used the micron-sized x-ray beam available at the ESRF-EBS to make detailed measurements of both the pressure distribution within the sample chamber and the uniaxial stress distribution in the Rh sample. Using a flash laser heating system, we have also studied Rh at elevated temperatures, where we see clear evidence of alloying between the Rh and the Pt pressure calibrant. This alloying is evident from both the 2D diffraction images and the integrated profiles and, as such, these data were not included in the determination of the Rh EoS.

Initial studies at the European XFEL have shown Rh to be an almost ideal laser heating coupler. Our determination of a thermal EoS for Rh should broaden its use in the future. To facilitate this, we have also determined a thermal EoS for Rh that is suitable for use within the DIOPTAS analysis suite.

#### ACKNOWLEDGMENTS

British Crown Owned Copyright 2024/AWE. This work was supported by Grant No. EP/R02927X/1 from the U.K. Engineering and Physical Sciences Research Council (EPSRC). We also acknowledge DESY (Hamburg, Germany), a member of the Helmholtz Association HGF, for the provision of experimental facilities. We would like to thank H-P. Liermann, K. Glazyrin, and T. Fedotenko for their assistance on the P02.2 beamline at PETRA III, and M. Mezouar and T. Poreba for their support on the ID27 beamline at ESRF-EBS. J.D.M is grateful to AWE for the award of CASE Studentship P030463429.

- 
- [1] I. M. Tougas, M. Amani, and O. J. Gregory, Metallic and ceramic thin film thermocouples for gas turbine engines, *Sensors* **13**, 15324 (2013).
- [2] S. Dey and G. C. Dhal, Applications of rhodium and ruthenium catalysts for co oxidation: An overview, *Polytechnica* **3**, 26 (2020).
- [3] A. Jiang, J. Chen, S. Liu, Z. Wang, Q. Li, D. Xia, and M. Dong, Intermetallic rhodium alloy nanoparticles for electrocatalysis, *ACS Appl. Nano Mater.* **4**, 13716 (2021).
- [4] *LASL Shock Hugoniot Data*, edited by S. P. Marsh (University of California Press, Berkeley, 1980).
- [5] K. Yusenko, S. Khandarkhaeva, T. Fedotenko, A. Pakhomova, S. Gromilov, L. Dubrovinsky, and N. Dubrovinskaia, Equations of state of rhodium, iridium and their alloys up to 70 GPa, *J. Alloys Compd.* **788**, 212 (2019).
- [6] D. Young, H. Cynn, P. Soderlind, and A. Lanza, Zero-kelvin compression isotherms of the elements  $1 < Z < 90$  to 100 GPa, *J. Phys. Chem. Ref. Data* **45**, 043101 (2016).
- [7] M. Frost, D. Smith, E. E. McBride, J. S. Smith, and S. H. Glenzer, The equations of state of statically compressed palladium and rhodium, *J. Appl. Phys.* **134**, 035901 (2023).
- [8] C. Cazorla, D. Alfè, and M. J. Gillan, Zero-temperature generalized phase diagram of the  $4d$  transition metals under pressure, *Phys. Rev. B* **77**, 224103 (2008).
- [9] D. C. Swift, T. Lockard, O. Heuze, M. Frost, S. Glenzer, K. J. McClellan, S. Hamel, J. E. Klepeis, L. X. Benedict, P. A. Sterne, and G. J. Ackland, Equations of state for ruthenium and rhodium, [arXiv:1909.05391](https://arxiv.org/abs/1909.05391).
- [10] H. P. Liermann, Z. Konôpková, K. Appel, C. Prescher, A. Schropp, V. Cerantola, R. J. Husband, J. D. McHardy, M. I. McMahon, R. S. McWilliams, C. M. Pépin, J. Mainberger, M. Roeper, A. Berghäuser, H. Damker, P. Talkovski, M. Foese, N. Kujala, O. B. Ball, M. A. Baron *et al.*, Novel experimental setup for megahertz X-ray diffraction in a diamond anvil cell at the High Energy Density (HED) instrument of the European X-ray Free-Electron Laser (EuXFEL), *J. Synchrotron Radiat.* **28**, 688 (2021).
- [11] M. J. Duff, P. G. Heighway, J. D. McHardy, A. D'Souza, R. S. McWilliams, J. S. Wark, and M. I. McMahon, Atomistic investigation of cavitation and ablation in tantalum foils under irradiation with x-rays approaching 5 keV, *Phys. Rev. B* **106**, 024107 (2022).
- [12] R. Boehler, New diamond cell for single-crystal x-ray diffraction, *Rev. Sci. Instrum.* **77**, 115103 (2006).
- [13] C. V. Storm, J. D. McHardy, M. J. Duff, S. G. MacLeod, I. O'Bannon, E. F., and M. I. McMahon, The stress state in bismuth to 298 GPa and its use as a pressure transmitting medium and pressure marker at multi-megabar pressures, *J. Appl. Phys.* **133**, 245904 (2023).
- [14] M. Mezouar, W. A. Crichton, S. Bauchau, F. Thurel, H. Witsch, F. Torrecillas, G. Blattmann, P. Marion, Y. Dabin, J. Chavanne, O. Hignette, C. Morawe, and C. Borel, Development of a new state-of-the-art beamline optimized for monochromatic single-crystal and powder x-ray diffraction under extreme conditions at the ESRF, *J. Synchrotron Radiat.* **12**, 659 (2005).
- [15] C. Prescher and V. B. Prakapenka, Dioptas: a program for reduction of two-dimensional x-ray diffraction data and data exploration, *High Press. Res.* **35**, 223 (2015).
- [16] Z. Konôpková, W. Morgenroth, R. Husband, N. Giordano, A. Pakhomova, O. Gutowski, M. Wendt, K. Glazyrin, A. Ehnés, J. T. Delitz, A. Goncharov, V. Prakapenka, and H.-P. Liermann, Laser heating system at the extreme conditions beamline, P02.2, PETRA III, *J. Synchrotron Radiat.* **28**, 1747 (2021).
- [17] A. Dewaele, M. Mezouar, N. Guignot, and P. Loubeyre, High melting points of tantalum in laser-heated diamond anvil cell, *Phys. Rev. Lett.* **104**, 255701 (2010).
- [18] M. Mezouar, R. Giampaoli, G. Garbarino, I. Kantor, A. Dewaele, G. Weck, S. Boccato, V. Svitlyk, A. D. Rosa, R. Torchio, O. Mathon, O. Hignette, and S. Bauchau, Methodology for in situ synchrotron x-ray studies in the laser-heated diamond anvil cell, *High Press. Res.* **37**, 170 (2017).
- [19] See Supplemental Material at <http://link.aps.org/supplemental/10.1103/PhysRevB.109.094113> for tabulated experimental data, details on the stress state analysis, tabulated elastic con-

- stants for Rh, tabulated isotherms for the thermal EoS, error propagation formulas for the AP2 equation, and details on the reduction of shock data performed for Rh. The Supplemental Material also includes Refs. [52–67].
- [20] J. Gonzalez-Platas, M. Alvaro, F. Nestola, and R. Angel, *EosFit7-GUI: A new graphical user interface for equation of state calculations, analyses and teaching*, *J. Appl. Crystallogr.* **49**, 1377 (2016).
- [21] V. Petříček, M. Dusek, and L. Palatinus, Crystallographic computing system jana2006: General features, *Z. Kristallogr.: Cryst. Mater.* **229**, 345 (2014).
- [22] Y. Akahama, H. Kawamura, and A. Singh, Equation of state of bismuth to 222 GPa and comparison of gold and platinum pressure scales to 145 GPa, *J. Appl. Phys.* **92**, 5892 (2002).
- [23] D. J. Campbell, D. T. Sneed, E. F. O’Bannon, P. Söderlind, and Z. Jenei, Refined room-temperature equation of state of Bi up to 260 GPa, *Phys. Rev. B* **107**, 224104 (2023).
- [24] A. K. Singh, The lattice strains in a specimen (cubic system) compressed nonhydrostatically in an opposed anvil device, *J. Appl. Phys.* **73**, 4278 (1993).
- [25] A. K. Singh, Erratum: “the lattice strains in a specimen (cubic system) compressed nonhydrostatically in an opposed anvil device”, *J. Appl. Phys.* **74**, 5920 (1993).
- [26] A. K. Singh and K. Takemura, Measurement and analysis of nonhydrostatic lattice strain component in niobium to 145 GPa under various fluid pressure-transmitting media, *J. Appl. Phys.* **90**, 3269 (2001).
- [27] K. Takemura and A. Dewaele, Isothermal equation of state for gold with a He-pressure medium, *Phys. Rev. B* **78**, 104119 (2008).
- [28] W. Holzapfel, Equations of state for solids under strong compression, *Z. Kristallogr.* **216**, 473 (2001).
- [29] Z. Shao, D. Duan, L. Wang, H. Song, H. Yu, Y. Yao, and T. Cui, First-principles investigation of rhodium hydrides under high pressure, *Phys. Rev. B* **104**, 054110 (2021).
- [30] R. F. Trunin, Shock compression of condensed materials (laboratory studies), *Phys. Usp.* **44**, 371 (2001).
- [31] E. Walker, J. Ashkenazi, and M. Dacorogna, Elastic moduli of rhodium: Correct prediction by a new theoretical method, *Phys. Rev. B* **24**, 2254 (1981).
- [32] J. Nye, *Physical Properties of Crystals: Their Representation by Tensors and Matrices* (Oxford University Press, Oxford, 1957).
- [33] X.-G. Lu, M. Selleby, and B. Sundman, Assessments of molar volume and thermal expansion for selected bcc, fcc and hcp metallic elements, *CALPHAD: Comput. Coupling Phase Diagrams Thermochem.* **29**, 68 (2005).
- [34] G. T. Furukawa, M. L. Reilly, and J. S. Gallagher, Critical Analysis of Heat—Capacity Data and Evaluation of Thermodynamic Properties of Ruthenium, Rhodium, Palladium, Iridium, and Platinum from 0 to 300 K. A Survey of the Literature Data on Osmium., *J. Phys. Chem. Ref. Data* **3**, 163 (1974).
- [35] W. B. Holzapfel, Equations of state for solids under strong compression, *High Press. Res.* **16**, 81 (1998).
- [36] S. Anzellini, D. Errandonea, C. Carzoria, S. MacLeod, V. Monteseguro, S. Boccato, E. Bandiello, D. D. Anitchenko, C. Popescu, and C. M. Beavers, Thermal equation of state of ruthenium characterized by resistively heated diamond anvil cell, *Sci. Rep.* **9**, (2019).
- [37] H. K. Mao, P. M. Bell, J. W. Shaner, and D. J. Steinberg, Specific volume measurements of Cu, Mo, Pd, and Ag and calibration of the ruby  $R_1$  fluorescence pressure gauge from 0.06 to 1 Mbar, *J. Appl. Phys.* **49**, 3276 (1978).
- [38] A. Dewaele, P. Loubeyre, and M. Mezouar, Equation of state of six metals above 94 GPa, *Phys. Rev. B* **70**, 094112 (2004).
- [39] D. E. Fratanduono, R. F. Smith, S. J. Ali, D. G. Braun, A. Fernandez-Pañella, S. Zhang, R. G. Kraus, F. Coppari, J. M. McNaney, M. C. Marshall, L. E. Kirch, D. C. Swift, M. Millot, J. K. Wicks, and J. H. Eggert, Probing the solid phase of noble metal copper at terapascal conditions, *Phys. Rev. Lett.* **124**, 015701 (2020).
- [40] C. V. Storm, J. D. McHardy, S. E. Finnegan, E. J. Pace, M. G. Stevenson, M. J. Duff, S. G. MacLeod, and M. I. McMahon, Behavior of rubidium at over eightfold static compression, *Phys. Rev. B* **103**, 224103 (2021).
- [41] E. J. Pace, S. E. Finnegan, C. V. Storm, M. Stevenson, M. I. McMahon, S. G. MacLeod, E. Plekhanov, N. Bonini, and C. Weber, Structural phase transitions in yttrium up to 183 GPa, *Phys. Rev. B* **102**, 094104 (2020).
- [42] S. E. Finnegan, E. J. Pace, C. V. Storm, M. I. McMahon, S. G. MacLeod, H.-P. Liermann, and K. Glazyrin, High-pressure structural systematics in samarium up to 222 GPa, *Phys. Rev. B* **101**, 174109 (2020).
- [43] T. Sokolova, P. Dorogokupets, and K. Litasov, Self-consistent pressure scales based on the equations of state for ruby, diamond, MgO, B2–NaCl, as well as Au, Pt, and other metals to 4 Mbar and 3000 K, *Russ. Geol. Geophys.* **54**, 181 (2013).
- [44] T. S. Sokolova, P. I. Dorogokupets, A. M. Dymshits, and B. S. Danilov, Microsoft excel spreadsheets for calculation of P–V–T relations and thermodynamic properties from equations of state of MgO, diamond and nine metals as pressure markers in high-pressure and high-temperature experiments, *Comput. Geosci.* **94**, 162 (2016).
- [45] H. M. Strong and F. P. Bundy, Fusion curves of four group viii metals to 100 000 atmospheres, *Phys. Rev.* **115**, 278 (1959).
- [46] S. Anzellini, V. Monteseguro, E. Bandiello, A. Dewaele, L. Burakovsky, and D. Errandonea, In situ characterization of the high pressure –high temperature melting curve of platinum, *Sci. Rep.* **9**, 13034 (2019).
- [47] R. H. Schroder, N. Schmitz-Pranghe, and R. Kohlaas, Experimental determination of the lattice parameters of the platinum metals and the equation of state of solids, *Z. Metallkde* **63**, 630103 (1972).
- [48] T. J. B. Holland and R. Powell, An improved and extended internally consistent thermodynamic dataset for phases of petrological interest, involving a new equation of state for solids, *J. Metamorph. Geol.* **29**, 333 (2011).
- [49] H. Kroll, A. Kirfel, R. Heinemann, and B. Barbier, Volume thermal expansion and related thermophysical parameters in the Mg,Fe olivine solid-solution series, *Eur. J. Mineralogy* **24**, 935 (2012).
- [50] R. J. Angel, M. Alvaro, and J. Gonzalez-Platas, Eosfit7c and a fortran module (library) for equation of state calculations, *Z. Kristallogr.: Cryst. Mater.* **229**, 405 (2014).
- [51] J. D. McHardy, C. V. Storm, M. J. Duff, S. G. Macleod, and M. I. McMahon, On the creation of thermal equations of state for use in dioplas, *High Press. Res.* **43**, 40 (2023).

- [52] A. K. Singh, C. Balasingh, H.-k. Mao, R. J. Hemley, and J. Shu, Analysis of lattice strains measured under nonhydrostatic pressure, *J. Appl. Phys.* **83**, 7567 (1998).
- [53] O. Degtyareva, M. I. McMahon, and R. J. Nelmes, High-pressure structural studies of group-15 elements, *High Press. Res.* **24**, 319 (2004).
- [54] K. M. Knowles and P. R. Howie, The directional dependence of elastic stiffness and compliance shear coefficients and shear moduli in cubic materials, *J. Elast.* **120**, 87 (2015).
- [55] A. Meurer, C. P. Smith, M. Paprocki, O. Čertík, S. B. Kirpichev, M. Rocklin, A. Kumar, S. Ivanov, J. K. Moore, S. Singh, T. Rathnayake, S. Vig, B. E. Granger, R. P. Muller, F. Bonazzi, H. Gupta, S. Vats, F. Johansson, F. Pedregosa, M. J. Curry *et al.*, Sympy: symbolic computing in python, *PeerJ Comput. Sci.* **3**, e103 (2017).
- [56] M. Cowperthwaite, Significance of some equations of state obtained from shock-wave data, *Am. J. Phys.* **34**, 1025 (1966).
- [57] B. Eisenmann and H. Schäfer, *Elements, Borides, Carbides, Hydrides* (6.1 elements) (Springer, Berlin, 1988).
- [58] K. Kelley, *High-temperature Heat-content, Heat-capacity, and Entropy Data for Inorganic Compounds*, Vol. 476 (US Government Printing Office, Washington, DC, 1949).
- [59] J. W. Forbes, in *Shock Wave Compression of Condensed Matter: A Primer*, edited by R. A. Graham (Springer, Berlin, 2012).
- [60] J. M. Walsh and R. H. Christian, Equation of state of metals from shock wave measurements, *Phys. Rev.* **97**, 1544 (1955).
- [61] G. Kresse and J. Hafner, Ab initio molecular dynamics for liquid metals, *Phys. Rev. B* **47**, 558 (1993).
- [62] G. Kresse and J. Furthmüller, Efficiency of ab-initio total energy calculations for metals and semiconductors using a plane-wave basis set, *Comput. Mater. Sci.* **6**, 15 (1996).
- [63] G. Kresse and J. Furthmüller, Efficient iterative schemes for ab initio total-energy calculations using a plane-wave basis set, *Phys. Rev. B* **54**, 11169 (1996).
- [64] G. Kresse and D. Joubert, From ultrasoft pseudopotentials to the projector augmented-wave method, *Phys. Rev. B* **59**, 1758 (1999).
- [65] J. P. Perdew, K. Burke, and M. Ernzerhof, Generalized gradient approximation made simple, *Phys. Rev. Lett.* **77**, 3865 (1996).
- [66] C. Prescher, E. Greenberg, N. Holtgrewe, and V. Prakapenka, T-rax (unpublished).
- [67] S. B. Segletes, Thermodynamic stability of the mie-gruneisen equation of state, and its relevance to hydrocode computations, *J. Appl. Phys.* **70**, 2489 (1991).